



HAL
open science

Magnetization mechanisms for non-destructive evaluation of low-carbon steels subject to early-stage low-temperature thermal oxidation

Anita Mongshi, Yves Armand Tene Deffo, Nicolas Mary, Pierre Tsafack, Jean-François Mognotte, Benjamin Ducharne

► **To cite this version:**

Anita Mongshi, Yves Armand Tene Deffo, Nicolas Mary, Pierre Tsafack, Jean-François Mognotte, et al.. Magnetization mechanisms for non-destructive evaluation of low-carbon steels subject to early-stage low-temperature thermal oxidation. *Journal of Magnetism and Magnetic Materials*, 2024, 612, pp.172643. 10.1016/j.jmmm.2024.172643 . hal-04806675

HAL Id: hal-04806675

<https://hal.science/hal-04806675v1>

Submitted on 27 Nov 2024

HAL is a multi-disciplinary open access archive for the deposit and dissemination of scientific research documents, whether they are published or not. The documents may come from teaching and research institutions in France or abroad, or from public or private research centers.

L'archive ouverte pluridisciplinaire **HAL**, est destinée au dépôt et à la diffusion de documents scientifiques de niveau recherche, publiés ou non, émanant des établissements d'enseignement et de recherche français ou étrangers, des laboratoires publics ou privés.

Magnetization mechanisms for non-destructive evaluation of low-carbon steels subject to early-stage low-temperature thermal oxidation

Anita Mongshi^{1,2}, Yves Armand Tene Deffo^{1,2*}, Nicolas Mary³, Pierre Tsafack^{1,2}, Jean-François Mognotte⁴ and Benjamin Ducharne^{4,5*}

¹Faculty of Engineering and Technology, University of Buea, Buea P.O. Box 63, Cameroon

²Laboratory of Electrical Engineering and Computing (LEEC), University of Buea, Buea P.O. Box 63, Cameroon

³Université de Lyon, CNRS, Université Claude Bernard Lyon 1, MATEIS, UMR5510, Villeurbanne, Cedex, 69621, France

⁴Univ Lyon, INSA Lyon, LGEF EA682, 69621 Villeurbanne, France

⁵ELyTMaX IRL3757, Univ Lyon, INSA Lyon, Centrale Lyon, Université Claude Bernard Lyon 1, Tohoku University, Sendai 980-8577, Japan

*Correspondence: yteneffo@yahoo.com, benjamin.ducharne@insa-lyon.fr

Abstract

In this work, an investigation is done to identify the magnetic non-destructive testing techniques and their related magnetization mechanisms and, eventually, the associated indicators that present the most distinguishable response to changes in steel properties due to the onset and evolution of starting corrosion by thermal oxidation at low temperatures. This is found by measuring magnetic responses of Magnetic Hysteresis Cycle (MHC), Magnetic Barkhausen Noise (MBN), and Magnetic Incremental Permeability (MIP) at the early stage of corrosion. Herein, the magnetization mechanism identified by the Domain Wall Bulging (DWB) effect and represented by the indicator $\Delta|Z|_{MIP}$ from the MIP response is ranked the most sensitive indicator by Pearson's linear correlation coefficient (LCC). It is immediately followed by the Domain Wall's Irreversible Motions (DWIM) represented by the MBN coercivity indicator. Both mechanisms are associated with the structure and kinetic of the magnetic domains, respectively, under low and medium magnetic excitations. The low-temperature thermal oxidation process set out the constructive effect of the oxide layer in the strain relief effect on the overall magnetic response of the corroded specimen. Discussions and conclusions are provided, as well as perspectives regarding the applicability of magnetic non-destructive testing techniques.

Keywords

Magnetic non-destructive testing, hysteresis cycle, Barkhausen noise, incremental permeability, degradation evaluation.

I - Introduction

Steel, an alloy of iron and carbon, is a fundamental material for various industries, including biomedical equipment [1], nuclear and chemical industries, construction [2], automotive, energy generation, and petrochemical sectors [3]. Its biodegradability, recyclability, and construction efficiency make it highly valuable [1]. However, steel is susceptible to corrosion, which degrades its properties when interacting with the environment [4].

Corrosion affects steel's mechanical and chemical properties, leading to equipment failures, production downtimes, and increased maintenance costs [4, 5]. This results in significant economic losses. Corrosion impacts composition, texture, thermal and electrical conductivity, and mechanical strength [5], causing structural damage, accidents, and environmental hazards [6]. The global cost of corrosion is estimated to be 3-4% of each nation's GDP [7].

Traditional corrosion detection methods, such as weight loss analyses [8], electrochemical analyses [9], ultrasonic testing, radiography, metallographic characterization, and optical sensing [10], have limitations. They can be time-consuming, destructive, inconsistent, and costly. Magnetic non-destructive testing methods (MNDTM) offer a promising alternative for characterizing the properties of steels.

Various magnetic responses, including the Magnetic Hysteresis Cycle (MHC) – magnetic flux density as a function of magnetic excitation field $B(H)$, Magnetic Barkhausen Noise (MBN), and Magnetic Incremental Permeability (MIP), have been studied [11-23]. Corrosion in carbon steel induces microstructural changes that correlate with magnetic and mechanical properties [24-26]. MNDTM has shown effectiveness in detecting rust and other corrosion forms [11, 27-37]. For instance, MBN features (such as; rms signals, number of pulses, peak-to-peak value, etc.) has been extensively used to assess corrosion damage artificially developed in a neutral salt spray atmosphere; either applied to a fully ferritic steel subjected to tensile stress [34] or low-alloyed steels of variable tensile strength [35-36], then subjected to uniaxial tensile stress in the rolling and transverse directions [37]. Although these investigations reveal frank dependence of MBN emissions on corrosion extent and the superimposed tensile stresses, this form of corrosion tends to be more severe, forming grain boundary oxidation, and deeper corrosion pits, and is nowhere near to the targeted early-stage corrosion herein presented.

Despite extensive research, no studies have focused on using magnetic responses to monitor early-stage corrosion by thermal oxidation. Recent works have demonstrated the feasibility of MNDTM for observing and characterizing surface treatments and defects, such as carburization and grinding burns [38-40]. By focusing on magnetization mechanisms, this approach shows less sensitivity to experimental conditions, making it suitable for early-stage corrosion assessment. Thermal oxidation and the chemical deterioration of metal due to heating, has been studied primarily at high temperatures (400°C to 1200°C) [41-44]. However, low-temperature thermal oxidation remains less explored, raising uncertainties about its microstructural interpretation and magnetic response [41]. Studies have shown varying results based on temperature and exposure time, highlighting the need for further investigation into early-stage corrosion characteristics [46-49].

This study aims to evaluate early-stage oxide formation and microstructural changes from a magnetic perspective. Six identical steel rods, along with eight pins cut from one rod, were subjected to physical and magnetic evaluations after progressive heat treatments at 185°C.

Magnetic properties and corrosion status were assessed, and Pearson’s LCC were calculated to determine correlations between magnetic indicators and corrosion states.

II – Experimental procedure

2.1 - Material heat treatment

A low-carbon steel bar (hypoeutectoid ferrite-perlite) was divided into six physically identical rod specimens to ensure consistency in composition, treatment, and history [50]. The material chemical composition and physical properties (extracted from the literature) are reported in Table 1 and Table 2, respectively. Each rod had a length of 100 mm and a diameter of 10 mm. One of the rods was cut out into eight pins of 10 mm length. The rods and pins were divided into three groups. The first group, called “control,” was kept untreated. This group included one rod and one pin. The other groups were submitted to thermal oxidation treatments at low temperatures, leading to surface and sub-surface starting corrosion. The thermal oxidation process entailed placing four rods and four pins in a cold oven, heating the oven to 185°C from room temperature at 0.088°C·s⁻¹ over a ramp of 31 minutes. Then, the rods and the pins were left to oxidize in the oven at a stable temperature of 185°C for 96 hours. After this period, the rods and the pins were left to cool rapidly at room temperature in open air. All the thermal oxidations were performed in atmospheric air. Two of the four rods and two of the four pins were again subjected to thermal oxidation for another 96 hours. After each session of thermal oxidation, magnetic tests and SEM image characterizations were carried out (on rods and pins respectively).

Tab. 1 - Material chemical composition.

Element	C	Si	Ni	Mn	Fe
Mass fraction wt.%	0.3	0.31	0.05	0.66	Balance

Tab. 2 - Physical properties of low carbon steel from literature.

Quantity	Value	Unit
Tensile Strength	400 – 550	MPa
Yield strength	220 – 250	MPa
Young’s Modulus	200	GPa
Hardness	120	MPa
Expansion Coefficient	10.8 - 12.5 *(10 ⁻⁶)	°C ⁻¹
Poisson's coefficient	0.29	-
Density	7.85	Kg·m ⁻³
Elongation	0.76	%
Heat capacity	0.49	kJ·kg ⁻¹ ·°C ⁻¹
Electrical resistivity	10 ⁻⁷ Ωm	Ωm
Thermal conductivity	17	W·m ⁻¹ ·K ⁻¹

The preference for 96-hour oxidation time steps was based on related research works [48][52], which highlight the influential effects of oxidation time on the oxidation kinetics at low oxidation temperature, 185°C. These thermal oxidation conditions effectively produced distinguishable oxygen weight increment (mass gain) and the early-stage corrosion required by this study.

Image characterizations were done on the pins' surfaces to verify the evolution of the surface composition precisely. Mass evaluation versus corrosion rate calculations were performed on the rods to provide evidence of corrosion. The dimensions of the pins and rods are depicted in Fig. 1 below.

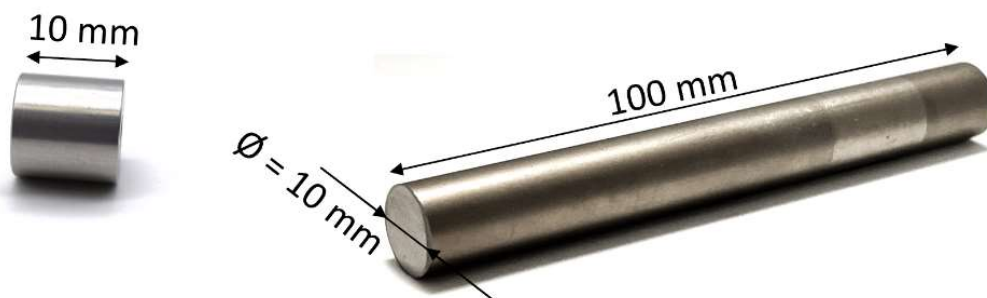


Fig. 1 - Rod and pin dimensions.

2.2 – Corrosion characterization

2.2.1 – Surface observation

The surface of the untreated pin was observed under a Scanning Electron Microscope (SEM – Supra 55VP, Zeiss, Oberkochen, Germany) at a one hundred times (x100) magnification before the first heat treatment process. This image was recorded and served as a reference. The metal's constitutive elements and their percentages by mass were also identified during this stage. Herein, a sample per heat treatment group and the reference sample were subject to the chemical analysis.

The SEM images were expected to show changes in the appearance of the surface texture [51]. Those changes served as physical proof of the corrosion process.

2.2.2 – Mass evaluation

Several approaches to the problem of predicting oxidation weight increment (mass gain) behavior exist in the literature [48][52]. These approaches however, differ based on the material type (composition and microstructure), the environmental conditions (dry or wet) and more importantly, oxidation temperature range (low, medium and high). Thus, investigating on early-stage corrosion pertains to low oxidation temperature range 100 – 300 °C.

Although the oxidation weight increment behaviors at this temperature range suggest no significant difference in the early hours of oxidation, Vernon et al [48] respectively observed a logarithmic and parabolic oxidation rates at temperatures below 200 °C and above 200 °C, for

100 hours of oxidation. The evidence of this empirical analysis has been further validated in subsequent research works [52].

According to [48], the total mass gain (w) during isothermal oxidation at 185°C can be approximated as a logarithmic function of the exposure time t as:

$$w = k_2 \log_{10}(at + 1) + b \quad (1)$$

Where k_2 , a , and b are constants. This equation is valid for a broad exposure time (up to 1400h). The oxidation rate constant (k_2) defines the oxidation rate in the logarithmic region below 200°C thermal oxidation and increases with increasing carbon content from 0.2 to 0.8 wt.% [52]. This rate constant k_2 for low-carbon steel with fine pearlite is 0.1 mg·cm⁻². a represents the inverse of the time constant (τ) that affects the shape and scale of the mass gain curve. It determines the rate at which the mass gain changes with respect to the logarithm of time. b is the additional mass gain due to the phase boundaries. It accounts for an initial film thickness of about 4 nm as a result of oxide formation at room temperature before thermal exposure while neglecting the metal surface roughness. In this study, a was set to 0.1 hours⁻¹, (i.e., $\tau = 10$ hours) and $b = 0.5 \mu\text{g}\cdot\text{cm}^{-2}$, when w is expressed in $\mu\text{g}\cdot\text{cm}^{-2}$ and t in hours. The following conditions were assumed;

- _ oxidation occurs uniformly across the surface of the metal,
- _ the same projected and actual surface areas,
- _ the oxide was assumed to be adherent to the metal surface.

Despite these assumptions aimed at minimizing uncertainty in the corrosion rate, errors due to time, dimensions, and mass measurements can still be sources of uncertainty. The logarithmic weight function effectively captures the rapid initial mass gain followed by a slowing rate as the oxide layer grows. It provides a realistic and useful description of the oxidation kinetics over a broad range of exposure times, including the first manifestations of the corrosion process.

2.3 – Magnetic characterization

In ferromagnetic materials, magnetic atomic moments are organized into regions called magnetic domains, each containing up to 10¹⁸ aligned magnetic moments [53, 54]. The orientation of these moments can change gradually over large numbers of atoms, forming domain boundaries or "domain walls" [55].

Magnetization mechanisms in ferromagnetic materials involve complex interactions such as exchange interactions between neighbouring atomic moments [56], the direction of the applied magnetic field, anisotropy degrees [57], thermal effects [58], and magneto-elastic contributions. These mechanisms are characterized by the movement and behaviour of domain walls in response to the applied magnetic field [38]. Initially, domains aligned with the applied field grow, while those unfavourably aligned shrink. The magnetization within the domains then rotates coherently toward the applied field direction.

The magnetization process, illustrated in Fig. 2, involves overlapping mechanisms during a magnetization cycle. These mechanisms can be categorized as follows:

Magnetization mechanisms related to magnetic domain dynamics [38]:

- _ Domain Wall Bulging (DWB, [21]): Reversible bending of domain walls under low magnetic excitation.

_ Domain Wall Irreversible Motion (DWIM): Irreversible movement of domain walls under medium magnetic excitation.

_ Domain Wall Dynamic Answer (DWDA): Frequency-dependent response associated with microscopic eddy currents.

_ Domain Nucleation and Fusion (DNF): Formation and merging of domains under high magnetic excitation.

Magnetization mechanisms related to atomic magnetic moments:

_ Magnetization Rotation (MR): Rotation of magnetic moments under high and very high magnetic excitation.

Macroscopic magnetization mechanisms:

_ Macroscopic Eddy Currents (MEC): Currents induced under dynamic magnetic excitation.

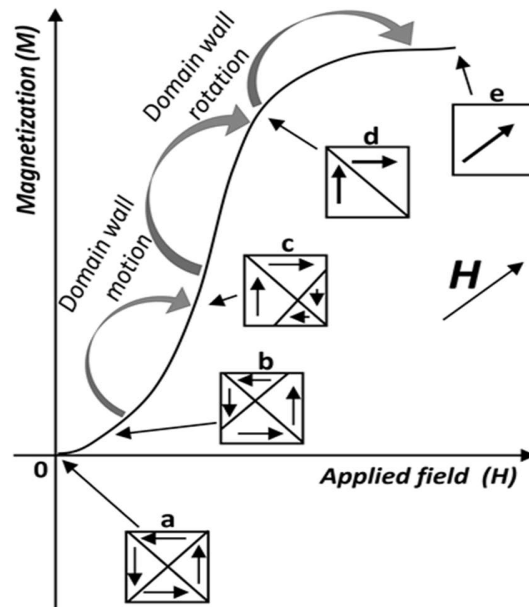


Fig. 2 - Schematic illustration of the magnetization process. (a) Demagnetized state (b) Magnetization onset (c) Domain wall motions (d) Magnetization rotation (e) Magnetization saturation. In practice, these mechanisms can coincide [59].

2.3.1 – Magnetic experimental characterization setup

- **Magnetic excitation**

Two U-shaped FeSi 3 wt.% yokes make up the magnetic inductor. The yokes have legs of dimensions 37 x 37 mm, designed 69 mm apart. Two steel spacers ensure the magnetic continuity between the tested rods and the yokes. A continuous excitation coil is wound around the yokes and supplied by a power amplifier (HSA 4014, NF Corporation, Yokohama, Japan) driven by a frequency generator (Agilent 33220A, Santa Clara, Ca, USA).

- **Magnetic sensors**

The rods for magnetic tests are slipped through 3D-printed support on which is wound two identical $n = 330$ turns sensor coils and a Hall element sensor (SS94A, Honeywell, 12 Charlotte, NC, USA). The Hall sensor measures the tangent magnetic field H_{surf} locally on the surface of the specimens. Both sensors plugged in series are used for magnetic measurement of $B_a(H_{surf})$ major hysteresis cycles (where B_a is the flux density averaged through the specimen cross-section) and Magnetic Incremental Permeability (MIP). Magnetic Barkhausen Noise (MBN) is measured by plugging the sensors in series opposition for natural filtering of the low-frequency signal contribution.

2.3.2 – $B_a(H_{surf})$ major hysteresis cycle

The voltage drop due to the magnetization variations is measured using the in-series wound coils and recorded with a Sirius® acquisition card (Dewesoft, Trbovlje, Slovenia). B_a is calculated using Eq. 2, after which drift correction is done to eliminate the undesirable effect of interference noise and errors due to integration calculations.

$$B_a = -\frac{1}{2n} \int_0^t e(t) dt \quad (2)$$

Where n is the coil number of turns, S is the cross-section area, and e is the electromotive force.

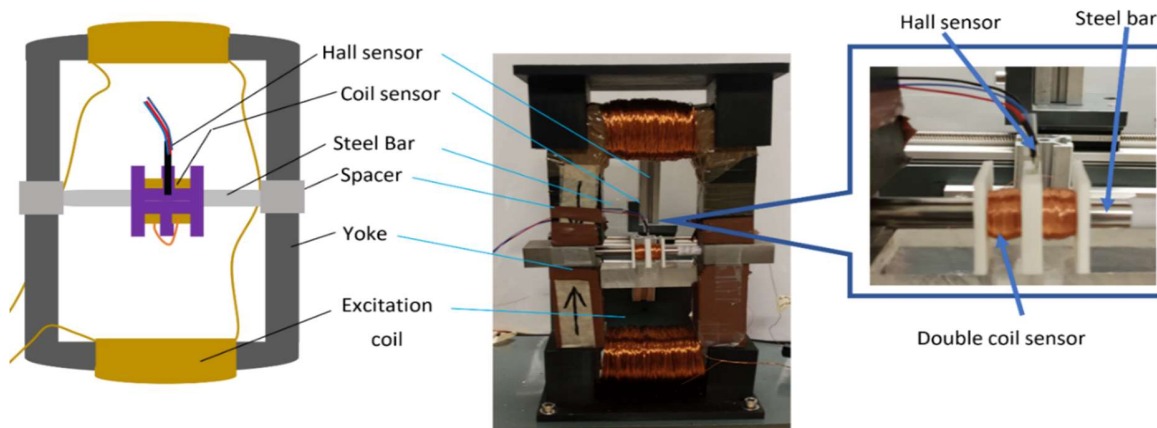


Fig. 3 - Excitation coil, yoke, spacers, steel bar sample, and sensors disposition.

2.3.3 – $MBN_e(H_{surf})$ hysteresis cycle

From prior research on the correlation between MBN and surface and subsurface material properties [60], its use in the search for changes due to heat treatment is justified. Nevertheless, Magnetic Barkhausen Noise (MBN) is stochastic [61]; thus, its pattern may be analyzed statistically but not precisely predicted. MBN_e (Eq. 3) obtained through integration over an entire period is much more reproducible and is recommended for deep analysis. Plotted as a function of H_{surf} , it gives rise to a hysteresis cycle depending on external mechanical conditions,

temperature, microstructural properties, and fatigue [60]. In this study, MBN_e was obtained in two steps:

_ The sensor coil electromotive force V_{MBN} was collected, filtered, and amplified using a Stanford Research SR650 (Sunnyvale, CA, USA). The cut-off frequencies were set to 1 and 50 kHz, and the gain to $90 \text{ dB}\cdot\text{dec}^{-1}$.

_ The square sensor coil electromotive force V_{MBN}^2 , its integration, and its drift correction were computed numerically using Matlab software.

NB: Data collection was done over five excitation periods.

$$MBN_e(t) = \int_0^t \text{sign}\left(\frac{dH_{surf}}{dt}\right) V_{MBN}^2 dt \quad (3)$$

[62] explains how MBN_e is not precisely energy but can be assimilated to an image of domain walls' kinetic energy.

2.3.4 – $Z_{MIP}(H_{surf})$, MIP butterfly loop

For ferromagnetic materials (including the low carbon steel studied in this work), the Magnetic Incremental Permeability (MIP) signature is measured by the superposition of a gradually changing high amplitude magnetic excitation to an Eddy Current Testing (ECT) characterization [23]. The butterfly loop refers to the measured incremental permeability plotted as a function of the quasi-static magnetic excitation field, which typically brings out a butterfly shape [23]. MIP is given by:

$$\mu_{MIP} = \frac{1}{\mu_0} \cdot \frac{\Delta B_a}{\Delta H_{surf}} \quad (4)$$

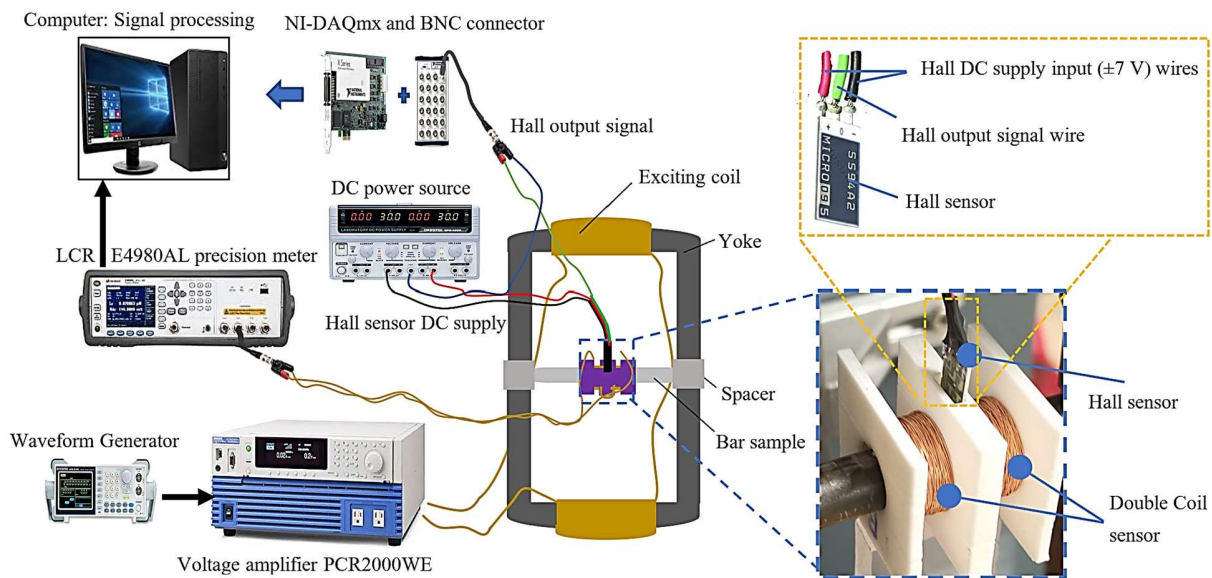


Fig. 4 - Magnetic experimental setup.

Where μ_0 represents the vacuum permeability, ΔH_{surf} a small variation of H_{surf} , and ΔB_a the relative variation of B_a . Figure 4 depicts an overall schematic representation of the magnetic characterization setup. MIP characterization is done by measuring the in-series connected coil sensor impedance through an LCR meter (LCR E4980AL precision meter, Keysight). The root mean square current passing through the coil sensor is kept at 10 mA. Data collected from the LCR meter at increasing frequencies (0.5 – 100 kHz) include the sensor coil impedance modulus, phase, and real and imaginary parts. This frequency range was set to assess the frequency that ensures significant penetration depth while keeping a usable signal.

2.3.5 – Magnetic indicators

A list of magnetic indicators read on the magnetic signatures ($B_a(H_{\text{surf}})$, $MBN_e(H_{\text{surf}})$, $|Z|_{\text{MIP}}(H_{\text{surf}})$) were selected for their privileged relationship with the magnetization mechanisms described above. Readers should refer to [38-40] for details about these relationships. All the coupled magnetization mechanisms/indicators are given in Table 3.

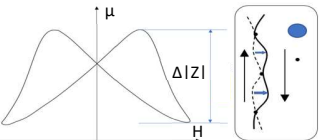
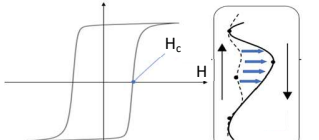
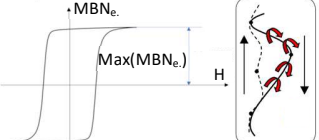
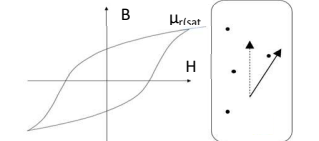
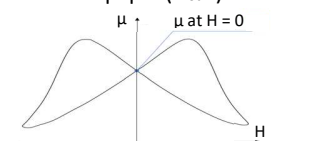
While the broad magnetization mechanisms (domain wall motion, pinning, hysteresis) are fundamentally similar, their response to different types of corrosion on low carbon steel can vary:

Under low-temperature thermal oxidation (generally below 250°C), the corrosion process often results in the formation of thin, stable oxide layers, such as ferrite ($\alpha\text{-Fe}_2\text{O}_3$) and potentially minor amounts of cementite. These oxides can alter the mechanical and magnetic properties of the material. Still, lower thermal energy levels lead to minimal changes in the material's microstructure and less aggressive degradation. Although the domain wall motion is still influenced by pinning sites created by microstructural anomalies, its impact on the magnetization mechanisms is deemed to be more subtle.

On the other hand, conventional corrosion takes place under more aggressive conditions, forming thicker oxide layers and more significant degradation of the microstructure. Herein, the pinning sites introduced by microstructural changes (such as oxidation of grain boundaries or increased porosity) are more pronounced. This leads to a more significant hindrance to domain wall motion, resulting in higher coercivity and more energy dissipation. Due to deeper structural degradation, the material's magnetic response may become more brittle, with increased hysteresis loss and a more pronounced impact on magnetic properties.

In summary, while the basic magnetization mechanisms (DWB, DWDA and DWIM) remain the same, their response to corrosion can differ in magnitude and nature depending on whether it is low-temperature or conventional thermal corrosion. Finally, there is no fundamental difference in the magnetization mechanisms' response; the differences lie more in how strongly these mechanisms are affected by the specific type of corrosion.

Tab. 3 - Magnetization mechanisms and their specific indicators [38].

Magnetization Mechanism	Definition	Magnetic Indicator Associated
Domain Wall Bulging - DWB	Domain wall bulging is a magnetization mechanism where the boundaries between magnetic domains, known as domain walls, expand or contract in response to a low-amplitude external magnetic field, causing limited and reversible changes in the overall magnetization of the material.	$\Delta Z - (MIP)$ 
Domain Wall's Irreversible Motions - DWIM	Domain wall irreversible motions refer to a magnetization mechanism where the boundaries between magnetic domains move permanently in response to an external magnetic field, leading to lasting changes in the material's magnetization.	Coercivity – $B_a(H_{surf})$, $MBN_e(H_{surf})$, and $ Z _{MIP}(H_{surf})$ 
Domains' Nucleation and Fusion – DNF	Magnetic domain nucleation and fusion is a magnetization mechanism where new magnetic domains are formed (nucleation), and existing domains merge (fusion) in response to an external magnetic field, altering the material's overall magnetization.	-
Domain Wall Dynamic Answer – DWDA	Domain wall dynamic response, or frequency dependency, is a magnetization mechanism where the movement of domain walls in a magnetic material varies with the frequency of the applied magnetic field, influencing the material's magnetic properties and behavior.	$\max(MBN_e) - (MBN)$ 
Magnetization Rotation – MR	Magnetization rotation is a magnetization mechanism where the direction of magnetic moments within a domain rotates in response to an external magnetic field, changing the overall magnetization of the material.	$\mu_{r(sat)} - (B_a(H_{surf}))$ 
Macroscopic Eddy Currents – MEC	Macroscopic eddy currents are a magnetization mechanism where circulating currents are induced in a conductive material in response to a changing magnetic field, generating their own magnetic fields and affecting the overall magnetization and energy dissipation within the material.	Remanence – $B_a(H_{surf})$, $MBN_e(H_{surf})$, and $ Z _{MIP}(H_{surf})$ 

NB DNF is not visible to human-scale magnetic characterization equipment [12].

III – Experimental results

3.1 – Corrosion characterization

3.1.1 – SEM observations

SEM images show the surface microstructure of all the specimen groups before and after different heat treatment exposure times, i.e., untreated (reference), 96 h, and 192 h heat-treated specimens (Fig. 5). The surface of the untreated specimen (or reference sample) has a hypoeutectoid ferrite-pearlite microstructure. The SEM analysis revealed the characteristic ferrite and pearlite features. The light and dark phases, respectively, were the ferrite and the pearlite. More precisely, the ferrite appears as relatively featureless light regions, and pearlite displays distinct bands (lamellar structure) of alternating ferrite and cementite. Iron carbide, rich in carbon, gives the dark appearance of Fig. 5a.

Then, after 96 h exposure time to 185 °C thermal oxidation, the early formation of a micaceous oxide film is observed at the surface of the 96 h heat-treated specimen. This oxide film consists of an outer layer of α -Fe₂O₃ overlying a very thin cubic oxide film (with a parameter structure appropriate to γ -Fe₂O₃ or Fe₃O₄ [48, 49]). The thickness of this trigonal oxide (α -Fe₂O₃), as well as the sizes of flakes (grain size), increase as the heat exposure time increases to 192 h as more oxygen ions diffuse through the oxide film, hence, more oxidation (Fig. 5c)[42].

Unlike the uniformly distributed oxide film and flakes observed after 96 h exposure, further exposure (2x96 h) to thermal oxidation results in inhomogeneity in the oxide film. Indeed, the formation of oxides at particular spots on the surface of the specimen releases electrons from one spot to another while reducing the oxygen level at the spots. This results in a relatively compacted oxide layer acting as a wear protection against further oxide formation.

The thermal oxidation is propagated predominantly by the diffusion of oxygen ions inwards (in the cubic oxide). This leads to a structure increasingly deficient in iron with increasing distance from the metallic base [48]. The virtual consistency of the film-derived oxides aligns with the sequence of colors, from the initial (reference) dull gray through straw (1 x 96 h) to deep straw (2 x 96 h).

As regards to the microstructural characterization, the nital attack and optical observation were used to identify the hypoeutectoid ferrite-pearlite microstructure of the low-carbon steel pins at room temperature. Herein, the samples' pins were etched with 2–3% nital for quantification of constitutive elements under optical microscopy. The respective mass fraction wt.% distribution of the constitutive elements per sample heat treatment group is captured in Fig. 5d. The rising percentage mass fraction of oxygen content with respect to the heat treatment time attest of the corrosion initiation and propagation in the samples.

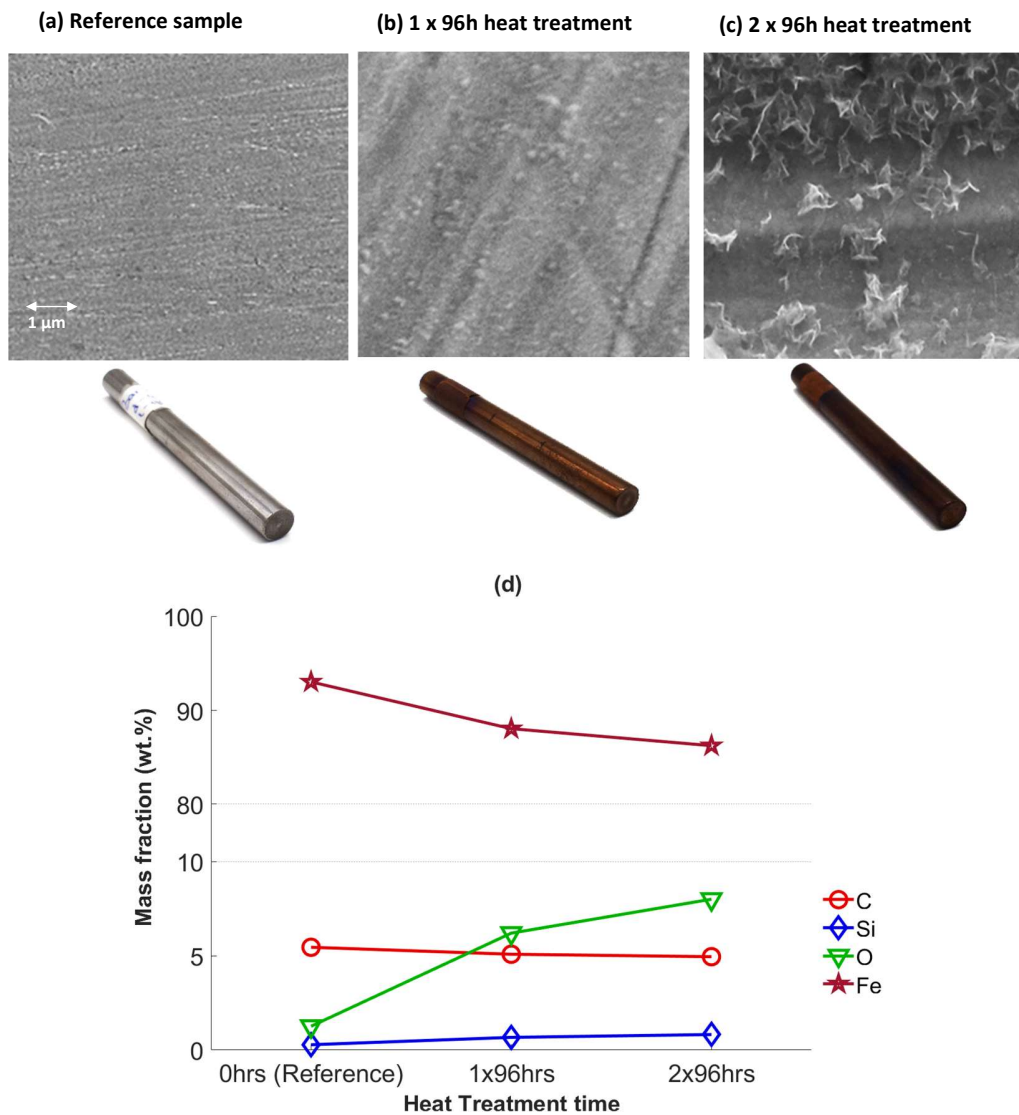


Fig. 5 – SEM images of all the specimens (at 100X); (a) Reference sample, (b) 1 x 96h heat treatment, (c) 2 x 96h heat treatment and (d) Mass fraction wt.% evolution per sample heat treatment group

3.1.2 – Mass evaluation

Fig. 6 presents mass gain ($\mu\text{g}\cdot\text{cm}^{-2}$) evolution for thermal oxidation performed in a laboratory furnace in dry air at 185°C . This figure reveals close agreement with the logarithmic weight increment function in Eq. 1 for an oxide-free surface [48].

Likewise, the oxidation-time curve shows a fast rise at early stages ($t < 100\text{h}$) of oxidation followed by a gentle increase at higher exposure time, confirming the earlier discussed oxide microstructure. The oxide depths per specimen versus exposure times are set out in Table 4. The highest corrosion depth occurs after 2 x 96 h of thermal oxidation ($3.6919\ \mu\text{m}$).

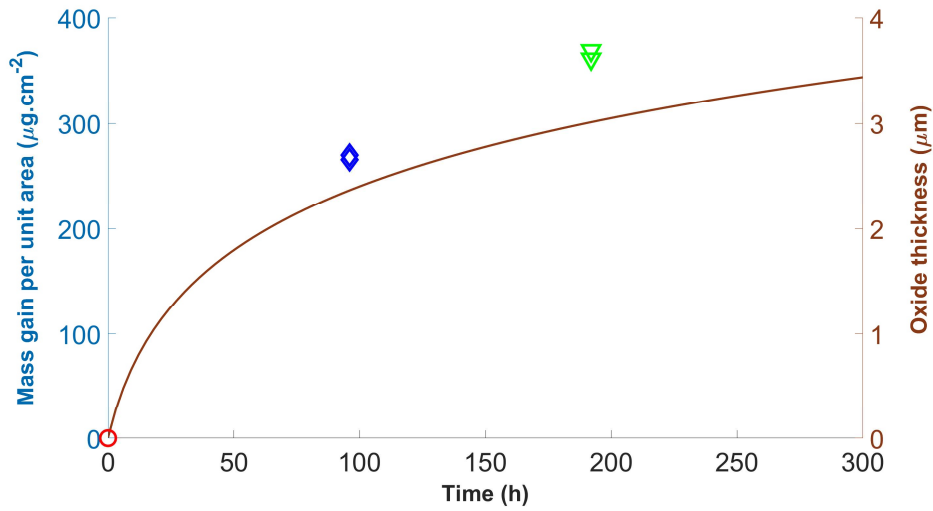


Fig. 6 - Mass gain and oxide thickness curves obtained during isothermal oxidation at 185°C.

Tab. 4 – Corrosion thickness with respect to exposure time.

Specimens	Exposure time (h)	Oxide thickness (µm)
1	0	0
2	96	2.6557
3	96	2.6997
4	2 x 96	3.6120
5	2 x 96	3.6919

3.2 – Magnetic characterization

The magnetic characterization of the different groups of specimens was performed using the experimental setup described in section 2.3.1 above (see Fig. 4). Herein, the three magnetic NDT methods (MHC, MBN, and MIP) were implemented for the same driving magnetic field strength (H_{surf}) and performed without any specific order. Using the same amplitude of H_{surf} ensures that the material reaches the same level of magnetic saturation in each test. This uniform saturation effectively resets the material's magnetic state, erasing any prior magnetic history or memory. Consequently, the order in which these tests are conducted becomes irrelevant, as each test starts with the material in a comparable magnetic state, ensuring consistent and repeatable results.

Fig. 7 below shows the magnetic signatures for all the samples with respect to the MHC and MBN methods. Each magnetic NDT method presents noticeable differences between each treatment group as reflected by their common magnetic indicators, such as the coercive field (H_c) and remanence field (Br).

A detailed analysis of these magnetic indicators' dependence on early-stage corrosion with respect to the magnetic NDT method is presented and further enhanced by the Pearson's LCC.

This coefficient measures the linear correlation between the measured corrosion depth (or oxide thickness) and the derived magnetic indicators for a given set of specimens. Indeed, the Pearson's LCC, r , is essentially a normalized measurement of the covariance of the magnetic indicator vector \mathbf{A} and the corrosion depth vector \mathbf{B} , each of N scalar observations (or specimens) such that the result always lies between -1 and 1 . It is expressed as follows:

$$\mathbf{r}(\mathbf{A}, \mathbf{B}) = \frac{1}{N-1} \sum_{i=1}^N \left(\frac{\mathbf{A}_i - \lambda_{\mathbf{A}}}{\sigma_{\mathbf{A}}} \right) \left(\frac{\mathbf{B}_i - \lambda_{\mathbf{B}}}{\sigma_{\mathbf{B}}} \right) \quad (5)$$

$$\mathbf{r}(\mathbf{A}, \mathbf{B}) = \frac{\text{cov}(\mathbf{A}, \mathbf{B})}{\sigma_{\mathbf{A}} \cdot \sigma_{\mathbf{B}}} \quad (6)$$

Where, $\lambda_{\mathbf{A}}$ and $\sigma_{\mathbf{A}}$ are the mean and standard deviation of \mathbf{A} , respectively, and $\lambda_{\mathbf{B}}$ and $\sigma_{\mathbf{B}}$ are the mean and standard deviation of \mathbf{B} . Note that only the magnitude of the Pearson's LCC, r , was considered hereafter for comparative analysis purpose.

- **$B_a(H_{\text{surf}})$ magnetic indicators analysis**

Fig. 8 depicts the evolution of the $B_a(H_{\text{surf}})$ indicators per specimen treatment group vs. the corrosion depth and their respective Pearson's LCC. It is obvious that the coercive field ($H_c - B_a(H_{\text{surf}})$) accounts for the most correlated $B_a(H_{\text{surf}})$ indicators to the measured corrosion depth with the highest Pearson's LCC of 0.752.

- **$MBN_e(H_{\text{surf}})$ magnetic indicators analysis**

Fig. 9 shows the evolution of the $MBN_e(H_{\text{surf}})$ indicators per specimen treatment group vs. the corrosion depth and their respective Pearson's LCC. In [63], it is explained that MBN_e is not precisely energy but can be assimilated to an image of domain walls' kinetic energy. Hence, its privileged relationship with the Domain Wall Dynamic Answer (DWDA), here represented by the $\max(MBN_e)$ indicator (Fig. 9c), spans the magnetization mechanisms of the MBN method. Unlike the $B_a(H_{\text{surf}})$ indicators analysis, two indicators – $\text{Rem}(MBN_e(H_{\text{surf}}))$ and $\max(MBN_e)$ – present the most correlated response to the starting corrosion profile with Pearson's LCC of 0.812 and 0.758, respectively. It is worth noting that the $MBN_e(H_{\text{surf}})$ indicators derived from the MBN response provide a higher average Pearson's LCC of 0.73 compared to 0.60 for the $B_a(H_{\text{surf}})$ indicators.

- **$|Z|_{\text{MIP}}(H_{\text{surf}})$ magnetic indicators investigation**

The MIP response allowed DWB (Domain Wall Bulging) measurement under low AC MIP signal amplitude to avoid DWIM (Domain Wall's Irreversible Motions). The observed increase in the impedance modulus (Fig. 9 and 10) with the development of an oxide or corrosion layer can be attributed to the contrasting effects of corrosion on electrical conductivity and magnetic properties. Specifically, corrosion reduces the material's electrical conductivity, leading to an increase in the real part of the impedance. While the degradation in magnetic properties from surface oxidation could reduce the reversible domain wall motion (potentially lowering the imaginary component of impedance), the dominant effect on the impedance modulus arises from the increased real component due to the conductivity decrease. This combined effect

results in an overall rise in impedance modulus, with conductivity degradation having a more substantial impact than the magnetic changes alone.

MIP measurements are commonly carried out at 50 kHz alternative contribution (according to the literature recommendation [63, 64]), although it has limited scanned depth due to electromagnetic skin effect (usually few μm for permeabilities in the range of the MIP measured ones).

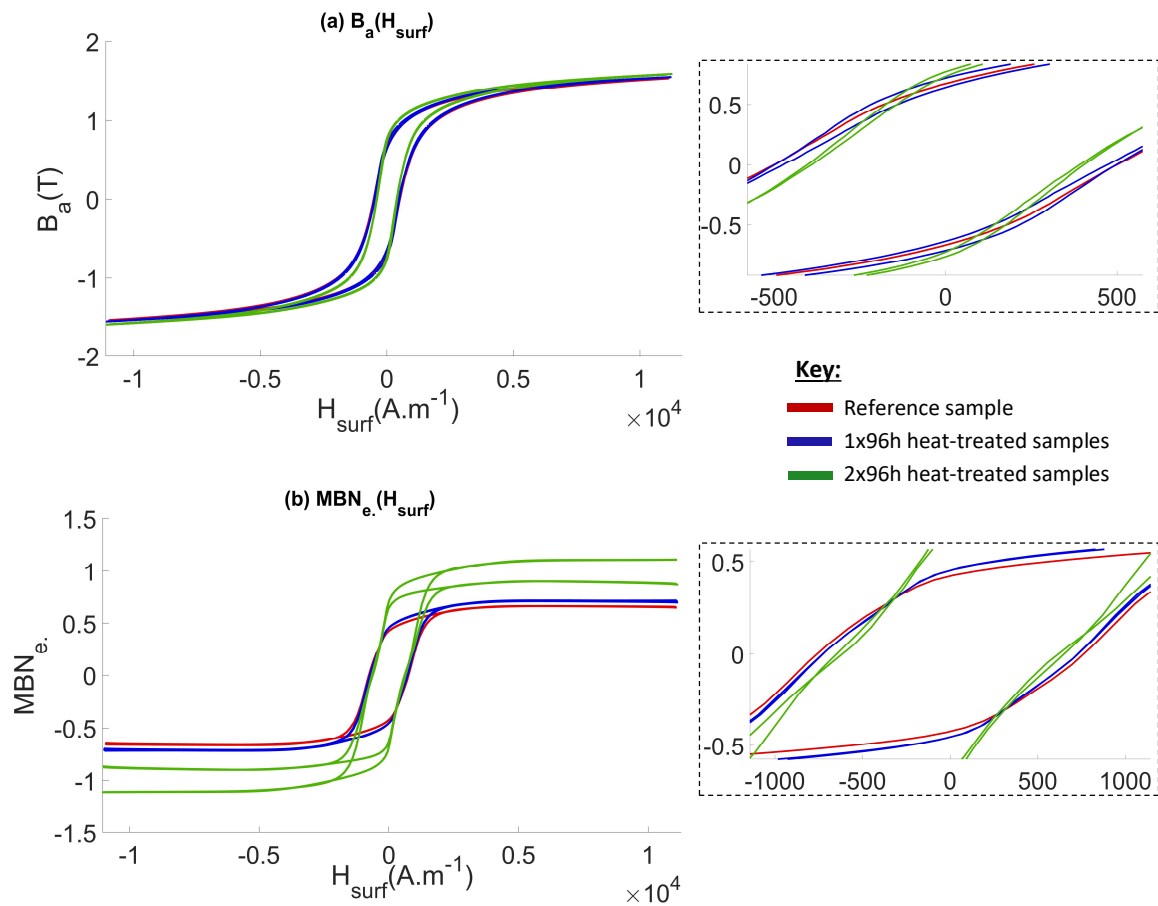


Fig. 7 - (a) $B_a(H_{\text{surf}})$ and (b) $MBN_e(H_{\text{surf}})$ respectively for all tested rods.

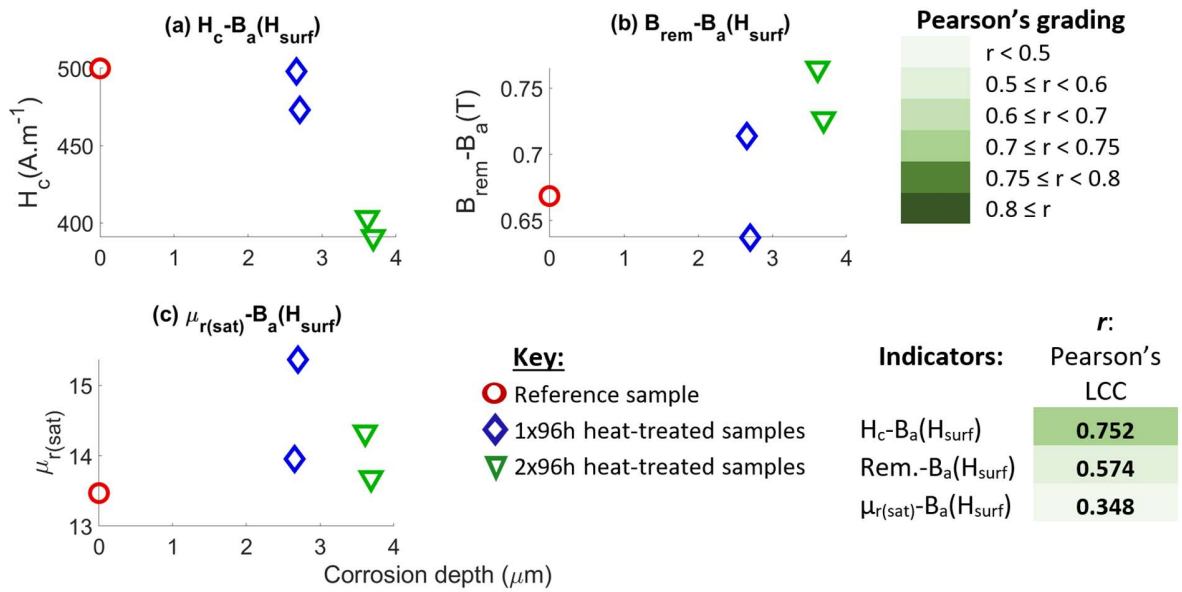


Fig. 8 - Comparison of the $B_a(H_{surf})$ indicators and Pearson's correlation coefficients with respect to the corrosion depth.

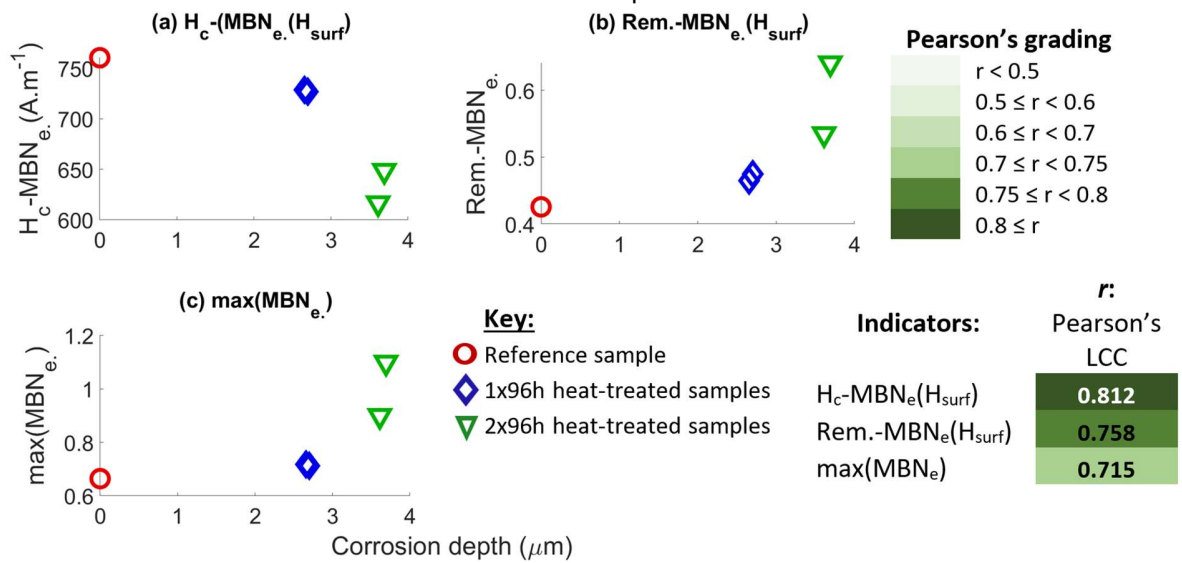


Fig. 9 - Comparison of the $MBN_e(H_{surf})$ indicators and Pearson's correlation coefficients vs. the corrosion depth.

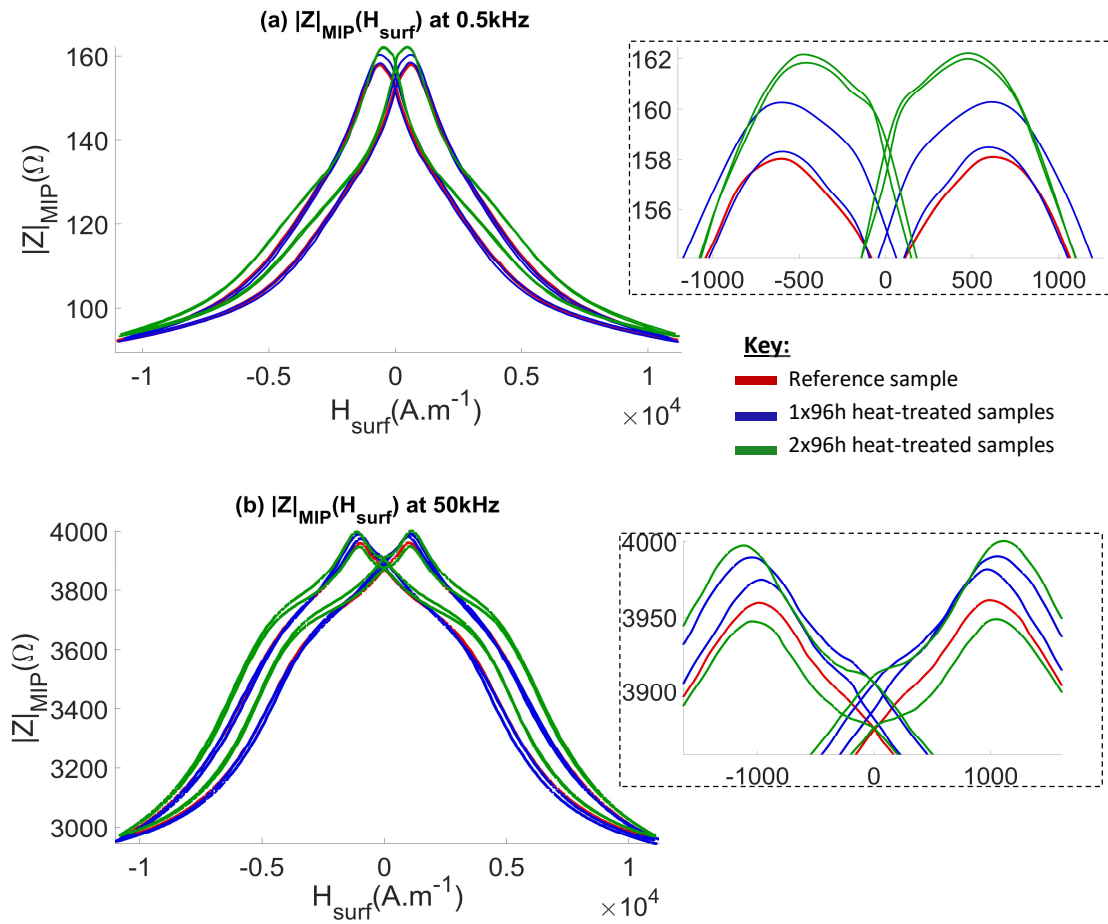


Fig. 10 - $|Z|_{MIP}(H_{surf})$ curves at (a) 0.5 kHz and (b) 50 kHz for all the specimens.

Hence, an increasing frequency analysis of the MIP alternative contribution was performed to determine the ideal low-frequency MIP response to extend the skin effect limit above the measured corrosion depth. Fig. 10 and 11, respectively, depict the MIP magnetic signatures and the MIP indicators' dependence on corrosion depth at 0.5 kHz and 50 kHz AC contributions.

The obvious dealignment of the magnetic signatures and the corresponding indicators' profile versus measured corrosion depth at 0.5 kHz and 50 kHz AC contributions tells of the intrinsic difference in scanning depth of the MIP measurements. Besides, MIP measurements at 0.5 kHz closely adhere to the MHC and MBN measurements above.

Likewise, the MIP indicators and Pearson's LCC dependency on the alternative contribution were evaluated for frequencies ranging from 0.5 to 100 kHz. The results are captured in Table 5.

One can conclude from the Pearson's LCC of increasing frequency analysis that only low-frequency ($f \leq 1$ kHz) alternative contributions allow to meet scanning depths beyond the measured corrosion depth. Thus, the MIP response perfectly accounts for the say "multiple-layer" that makes up the heat-treated specimens. This consists of the heat-induced surface hematite layer overlying the cubic oxide layer (upper layer) and the untreated sublayer of the specimen (below the measured corrosion depth).

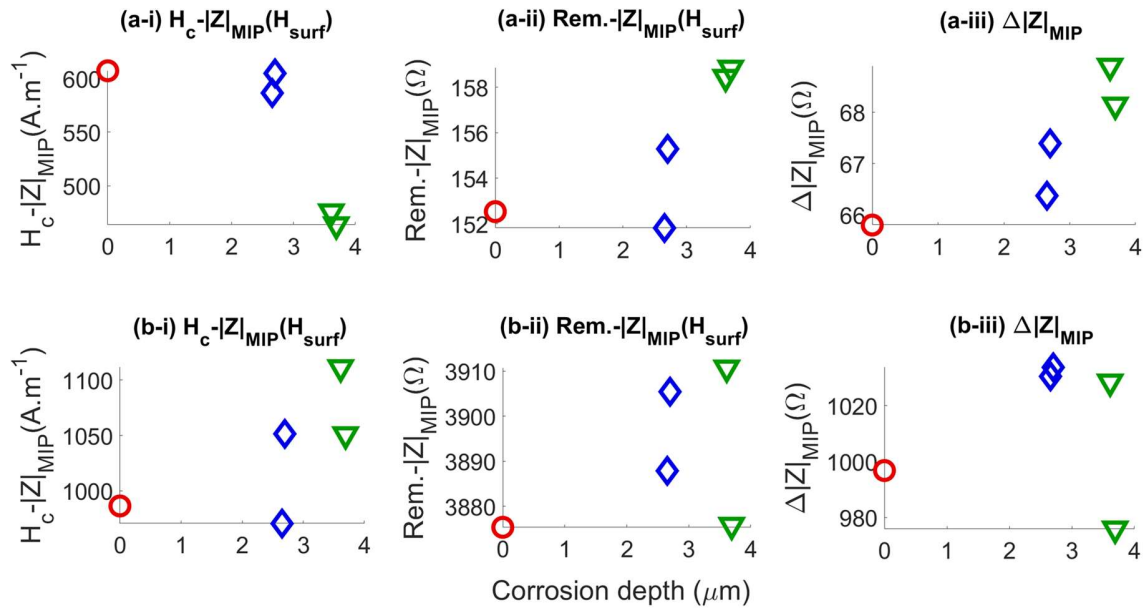


Fig. 11 - Comparison of the $|Z|_{MIP}(H_{surf})$ indicators at (a) 0.5 kHz and (b) 50 kHz and Pearson's correlation coefficients with respect to the corrosion depth.

Other sublayers may be unveiled, to wit, a “mixed region” iron with minimum oxide nuclei (transition layers) as observed in [47]. The postulate of a resultant “multiple-layer” in the heat-treated specimen is equally validated by the change in slope visible on the $|Z|_{MIP}(H_{surf})$ curves in Fig. 10. This sudden local change in slope appeared to be highly correlated to the metal treatment processes as described in [38] for carburization treatment of steel parts. Hence, one may conclude that the MIP increasing frequency analysis could eventually be used to determine the thickness of the oxide layer during the corrosion process.

Tab. 5 – $|Z|_{MIP}(H_{surf})$ indicators and Pearson's LCC vs. the corrosion depth for different alternative contribution frequencies.

Pearson's grading	Magnetic Indicators:	r : Pearson's LCC				
		0.5 kHz	1 kHz	10 kHz	50 kHz	100kHz
$r < 0.5$	$H_c- Z _{MIP}(H_{surf})$	0.726	0.732	0.532	0.644	0.356
$0.5 \leq r < 0.6$	$Rem.- Z _{MIP}(H_{surf})$	0.723	0.707	0.255	0.46	0.572
$0.6 \leq r < 0.7$	$\Delta Z _{MIP}$	0.846	0.667	0.055	0.133	0.409
$0.7 \leq r < 0.75$						
$0.75 \leq r < 0.8$						
$0.8 \leq r$						

3.3 – Analysis of the Pearson's correlation coefficients and magnetization mechanism derived indicators with vs. corrosion depth

A summary of the Pearson's LCC and magnetization mechanisms derived indicators vs. corrosion depth is presented in Table 6. This table allows us to compare the magnetic responses of each MNDTM as observed from their respective magnetization mechanisms. It also enables us to identify the most sensitive indicator per magnetization mechanism from the Pearson's LCC vs. corrosion depth analysis, as illustrated in Fig. 12.

Tab. 6 – Pearson's LCC and magnetic indicators vs. corrosion depth.

Magnetization Mechanism	Magnetic Indicator Associated	r: Pearson's LCC
Domain Wall Bulging - DWB	$\Delta Z - Z _{MIP}(H_{surf})$	0.846
Domain Wall's Irreversible Motions - DWIM	Coercivity – $B_a(H_{surf})$	0.752
	Coercivity – $MBN_e(H_{surf})$	0.812
	Coercivity – $ Z _{MIP}(H_{surf})$	0.726
Domains' Nucleation and Fusion – DNF	-	-
Domain Wall Dynamic Answer – DWDA	$\max(MBN_e) - MBN_e(H_{surf})$	0.715
Magnetization Rotation – MR	$\mu_{r(sat)} - B_a(H_{surf})$	0.348
Macroscopic Eddy Currents – MEC	Remanence – $B_a(H_{surf})$	0.574
	Remanence – $MBN_e(H_{surf})$	0.758
	Remanence – $ Z _{MIP}(H_{surf})$	0.723

Herein, the magnetization mechanism identified by the Domain Wall Bulging (DWB) effect and represented by the indicator $\Delta|Z|_{MIP}$ from the MIP response is ranked the most sensitive indicator by the Pearson's LCC vs. corrosion depth at 0.5 kHz AC contribution. It is immediately followed by the Domain Wall's Irreversible Motions (DWIM) represented by the MBN coercivity indicator (H_c - $MBN_e(H_{surf})$). These magnetization mechanisms are associated with the structure and kinetics of the magnetic domains, respectively, under low and medium magnetic excitations.

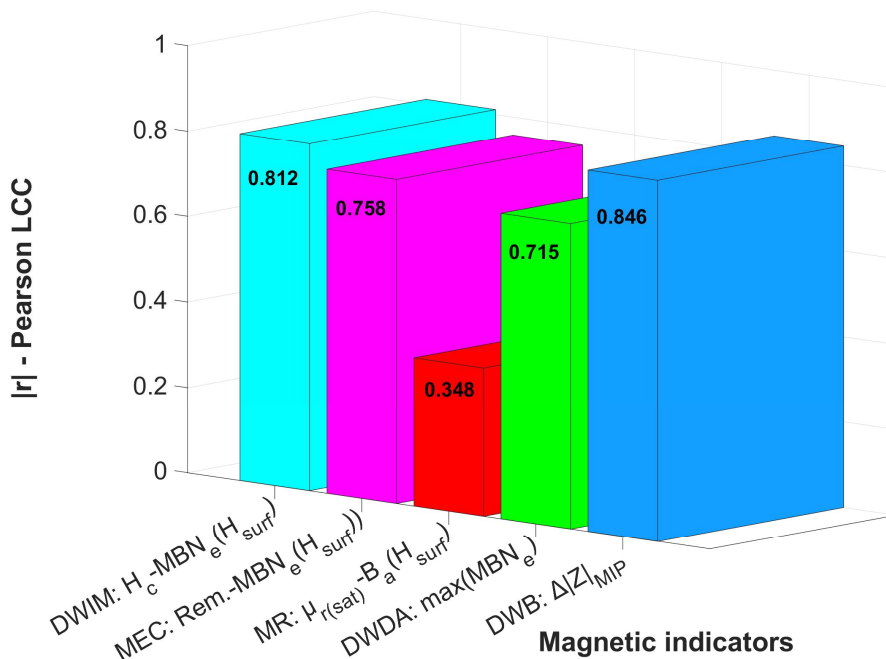


Fig. 12 - Most sensitive magnetic indicators, magnetization mechanisms, Pearson's LCC, vs. corrosion depth.

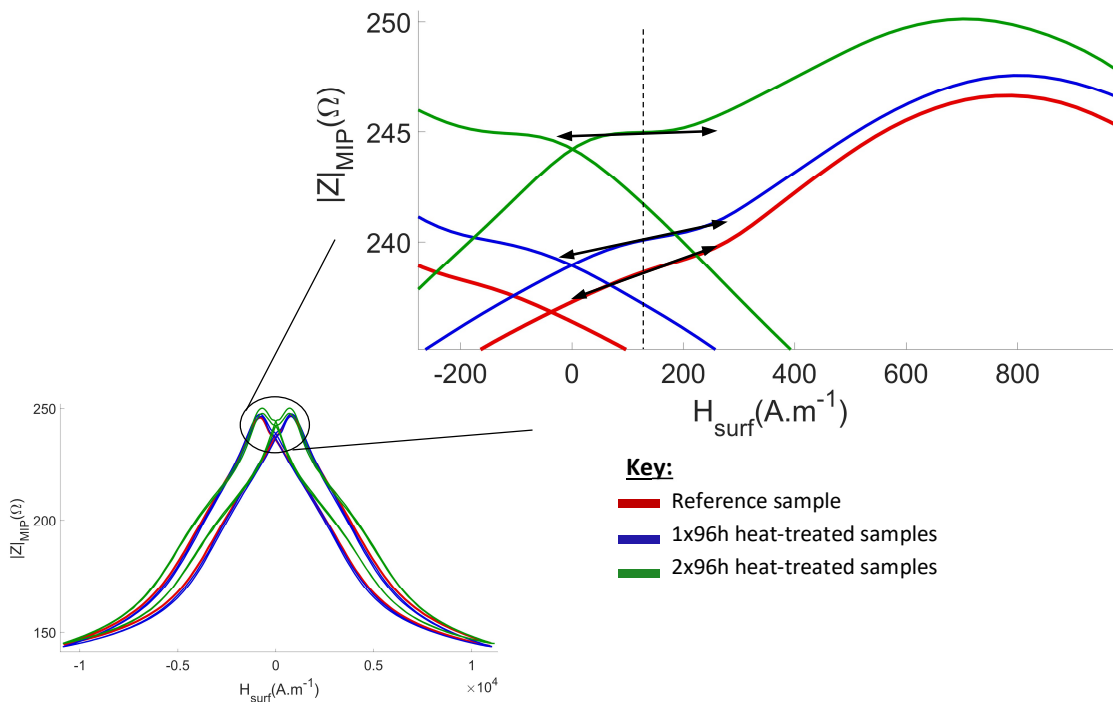


Fig. 13 - $|Z|_{MIP}(H_{surf})$ slope ($d|Z|_{MIP}/dH_{surf}$) at the inflection point due to slope change.

The domain walls' motion is generally subjected to microstructural impediments attributed to microstructural anomalies. These microstructural impediments act as pinning sites that hinder the smooth movement of domain walls, requiring higher applied magnetic fields to overcome

these obstacles. The interaction between the domain walls and these defects leads to energy dissipation and affects the overall magnetic properties of the material, such as coercivity and hysteresis loss. The coercivity per sample treated group, hence, the average pinning field, decreases as the exposure time increases (see Figures 8a, 9a, and 11a). This is because thermal oxidation at higher exposure time enhances the formation of oxides of lamellar pearlite.

Pearlite is a stable microconstituent lamella combination of alternate layers of predominantly ferrite (or α -Fe₂O₃) and little cementite, which respectively exhibit magnetically soft properties and magnetic inclusions to the pinning of domain walls at low temperatures (below 250°C)[65].

The mechanical properties of the lamellar pearlite are, thus, intermediate between those of ferrite (soft and ductile) and cementite (hard and brittle) [66]. The low-temperature thermal oxidation process set out the constructive effect of the oxide layer in the strain relief effect, resulting in softer steel both mechanically and magnetically. In addition, thermal noise at low heat treatment temperatures makes it easier to overcome pinning energy barriers due to the little decomposition of cementite, reducing the pinning field [67]. The magnetic responses and coupled indicators reveal this constructive effect of the oxide layer in the strain relief effect at low temperatures.

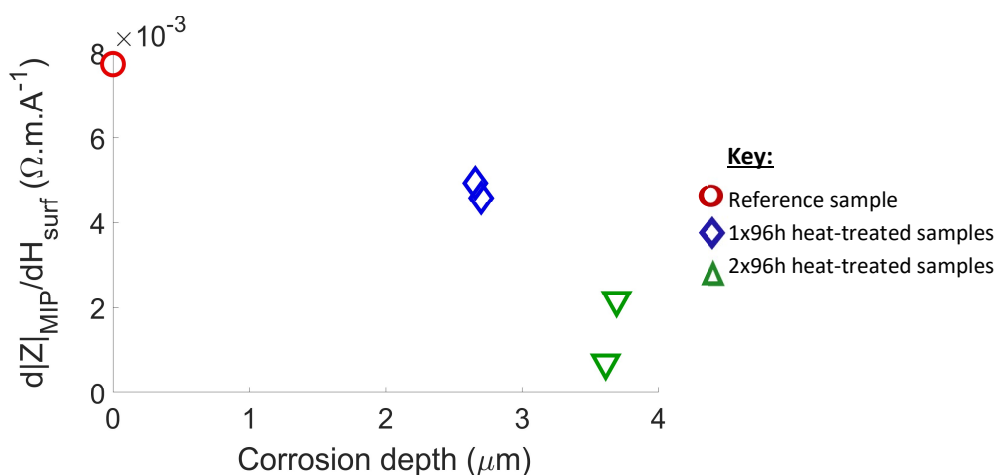


Fig. 14 - $|Z|_{\text{MIP}}(H_{\text{surf}})$ slope ($d|Z|/dH_{\text{surf}}$) at point of inflection vs. corrosion depth.

Tab. 7 – Pearson’s LCC for $d|Z|/dH_{\text{surf}}$ vs. corrosion depth at 1kHz at point of inflection.

New Indicators:	r : Pearson’s LCC at 1 kHz
$d Z _{\text{MIP}}/dH_{\text{surf}}$ at point of inflection	0.917

Moreover, the $|Z|_{\text{MIP}}(H_{\text{surf}})$ curves at a low applied magnetic field ($0 < H_{\text{surf}} < 200 \text{ A} \cdot \text{m}^{-1}$, see Fig. 10a) show a sudden local change in slope (rising point of inflection) for all the specimens. It is further observed that these slope changes follow a downward trend from the untreated specimen to the longest heat-treated specimen. Hence, by drawing a line common to all the specimen groups, a new indicator, $d|Z|_{\text{MIP}}/dH_{\text{surf}}$, is derived, where H_{surf} is defined as the applied

magnetic field measured at the rising point of inflection due to the sudden change in slope observed on all the specimens (see Fig. 13).

Low excitation magnetic field during the magnetization process is associated with the Domain Wall Bulging (DWB) effect, characterized by a high time constant and reversible local distortion of the magnetic domain walls. This mechanism, enhanced by the increasing oxygen content due to surface oxidation (see Fig. 5d), triggers a sudden bump in the measured impedance proportional to the extent of the microstructural anomalies (oxidized surface or corrosion depth). The inflection point around $H_{\text{surf}} \approx 100 \text{ A.m}^{-1}$ corresponds to the approximate coercivity of the softer, uncorroded inner material, while the corroded surface layer, being magnetically harder, has a higher coercivity around 700 A.m^{-1} (see Fig. 13). The impedance change at this low magnetic field primarily reflects the combined response of these layers, with each layer's influence depending on its thickness and magnetic properties. This results in an inflection point at very low applied magnetic fields ($0 < H_{\text{surf}} < 200 \text{ A.m}^{-1}$).

Thus, the low-frequency MIP signature is more of a stimulus for the DWB effect throughout the entire magnetization cycle, where $\Delta|Z|_{\text{MIP}}$ and $d|Z|_{\text{MIP}}/dH_{\text{surf}}$ at the point of inflection are fair indicators of this effect. The observed inflection point represents the combined magnetic responses of the corroded and uncorroded layers, which vary with the extent of oxidation. The evolution of this new indicator with respect to the corrosion depth per specimen heat treatment group and its respective Pearson's LCC are presented in Fig. 14. The $d|Z|_{\text{MIP}}/dH_{\text{surf}}$ at this point of inflection due to the sudden change in slope stands out as the most linearly correlated indicator vs. corrosion depth according to the Pearson's LCC (i.e., **0.917**).

IV – Conclusions

This work focused on detecting the onset of early-stage corrosion and studying its evolution on low-carbon steel. Cylindrical-shaped rods treated at different heat corrosion durations at 185°C were tested using various magnetic signatures. Testing a broad set of magnetic characterization methods was essential for collecting comprehensive magnetic information. Magnetic indicators were determined as key representatives of the magnetization mechanisms of the characterized MNDTM and tested against corrosion depth. By using specimens from the same steel bar; ensuring identical composition, treatment and history, and emphasizing on magnetization mechanisms, the study achieve more reliable detection regardless of variations in testing environments or conditions.

The key findings include:

_ First of all, emphasizing on magnetization mechanisms as new impetuses to derived magnetic indicators led to more reliable detection, regardless of variations in testing environments or conditions.

_ Then, linear correlations between magnetic indicators and corrosion depth have identified $\Delta|Z|_{\text{MIP}}$ from the low-frequency MIP signature as the most correlated indicator (0.846). This indicator is associated with Domain Wall Bulging, a magnetization mechanism highly linked to the measured surface oxidation (or corrosion depth) and hence, the microstructural evolution of the steel samples.

_ Further investigation of $|Z|_{\text{MIP}}(H_{\text{surf}})$ curves led to the development of a new indicator, $d|Z|_{\text{MIP}}/dH_{\text{surf}}$ at the point of inflection, with the highest Pearson's LCC of 0.917.

Other implications of these findings can be listed as:

- _ This study establishes low-frequency MIP as a powerful magnetic signature for early-stage corrosion evaluation of steel parts.

- _ Despite identifying low-frequency MIP as a highly responsive magnetic signature, the limited specimen set and number of tests necessitate further investigation across diverse specimen types and geometries.

Future work should address the following points:

- _ Exploring different thermal oxidation configurations, ranging from early-stage corrosion strain relief at low thermal oxidation to oxide layer flaking at high temperatures due to stress from thermal expansion differences.

- _ Considering other corrosion-induced processes, such as electrolysis, to validate the derived indicators in new configurations.

Finally, future applications of this research include:

- _ The magnetic signatures and indicators derived from MIP increasing frequency analysis could potentially determine the thickness of the oxide layer.

- _ Estimating the heat treatment trajectory during the corrosion process.

References

- [1] O. S. Putri and Firmansyah, "The Efficiency of Steel Material as Buildings Construction," *IOP Conf. Ser.: Mater. Sci. Eng.*, vol. 879, no. 1, p. 012148, 2020.
- [2] H. M. Cobb, "The history of stainless steel," *ASM International*, 2010.
- [3] M. Talha, C. K. Behera and O. P. Sinha, "A review on nickel-free nitrogen containing austenitic stainless steels for biomedical applications," *Materials Science and Engineering: C*, vol. 33, no. 7, p. 3563–3575, 2013.
- [4] B. Shaw and R. Kelly, "What is Corrosion?," *Electrochem. Soc. Interface*, vol. 15, no. 1, p. 24–26, 2006.
- [5] O. Juan, K. Viatcheslav and P. Dario, "Effects of Corrosion on the Microstructure, Hardness, and Microhardness of ASTM A335 P92 Steel," *Chemical Engineering Transactions*, vol. 76, p. 511–516, 2019.
- [6] Z. D. Lang, H. Liu and X. Gou, "Mapping the knowledge domains of research on corrosion of petrochemical equipment: An informetrics analysis-based study," *Engineering Failure Analysis*, vol. 129, p. 105716, 2021.
- [7] G. Koch, *Cost of corrosion in Trends in Oil and Gas Corrosion Research and Technologies*, Elsevier, 2017, p. 3–30.
- [8] P. McIntyre and A. Mercer, *Corrosion Testing and Determination of Corrosion Rates*, Elsevier, 2010.
- [9] A. Berradja, *Electrochemical Techniques for Corrosion and Tribocorrosion Monitoring: Methods for the Assessment of Corrosion Rates*, IntechOpen, 2019.
- [10] A. Al'khimenko, A. Davydov and al, "Methods of Corrosion Testing Used for the Development and Industrial Utilization of Novel Shipbuilding Steels and Alloys," *Steel Transl.*, vol. 52, no. 3, p. 271–277, 2022.
- [11] Y. Gotoh, H. Hirano, M. Nakano and al, "Electromagnetic non-destructive testing of rust region in steel," in *INTERMAG Asia: IEEE*, Nagoya, 2005.
- [12] S. Bi, A. Sutor, R. Lerch and Y. Xiao, "A measurement setup for acquiring the local magnetic properties of plastically deformed soft magnetic materials," *Journal of Applied Physics*, vol. 109, no. 7, p. 07E306, 2011.
- [13] A. Ktena, "Physics and Modeling of Magnetic Non Destructive Testing Techniques," *KEM*, vol. 495, p. 265–268, 2011.
- [14] O. Stupakov, "Controllable Magnetic Hysteresis Measurement of Electrical Steels in a Single-Yoke Open Configuration," *IEEE Trans. Magn.*, vol. 48, no. 12, p. 4718–4726, 2012.
- [15] M. P. van der Horst, M. L. Kaminski and E. Puik, "Methods for Sensing and Monitoring Fatigue Cracks and Their Applicability for Marine Structures," in *The Twenty-third International Offshore and Polar Engineering Conference*, 2013.
- [16] O. Stupakov, R. Wood, Y. Melikhov and D. Jiles, "Measurement of Electrical Steels With Direct Field Determination," *IEEE Trans. Magn.*, vol. 46, no. 2, p. 298–301, 2009.
- [17] O. Stupakov and Y. Melikhov, "Influence of Magnetizing and Filtering Frequencies on Barkhausen Noise Response," *IEEE Trans. Magn.*, vol. 50, no. 4, p. 1–4, 2014.
- [18] A. Stupakov, O. Perevertov and V. Zablotskii, "A system for controllable magnetic measurements of hysteresis and Barkhausen noise," in *2015 IEEE International Instrumentation and Measurement Technology Conference (I2MTC) Proceedings*, Pisa, Italy, 2015.
- [19] B. Ducharne, Y. A. Tene Deffo, P. Tsafack and S. Nguedjang Kouakeuo, "Directional magnetic Barkhausen noise measurement using the magnetic needle probe method'," *Journal of Magnetism and Magnetic Materials*, vol. 519, p. 167453, 2021.
- [20] H. E. Chen, X. S., H. Zhou, Z. Chen, T. Uchimoto, T. Takagi and Y. Kensuke, "Numerical simulation of magnetic incremental permeability for ferromagnetic material," *International Journal of Applied Electromagnetics and Mechanics*, Vols. 45(1-4), pp. 379-386, 2014.

- [21] B. Gupta, T. Uchimoto, B. Ducharne, G. Sebald, T. Miyazaki and T. Takagi, "Magnetic incremental permeability non-destructive evaluation of 12 Cr-Mo-W-V steel creep test samples with varied ageing levels and thermal treatments," *NDT & E International*, vol. 104, p. 42–50, 2019.
- [22] B. Gupta, B. Ducharne, G. Sebald, T. Uchimoto, T. Miyazaki and T. Takagi, "Physical interpretation of the microstructure for aged 12 Cr-Mo-W-V steel creep test samples based on simulation of magnetic incremental permeability," *Journal of Magnetism and Magnetic Materials*, vol. 486, p. 165250, 2019
- [23] S. Zhang, B. Ducharne, S. Takeda, S. Sebald and T. Uchimoto, "Identification of the ferromagnetic hysteresis simulation parameters using classic non-destructive testing equipment," *Journal of Magnetism and Magnetic Materials*, vol. 531, p. 167971, 2014.
- [24] Z. Babasafari, A. V. Pan, F. Pahlevani, C. Kong, M. Du Toit and R. Dippenaar, "Effect of Microstructural Features on Magnetic Properties of High-Carbon Steel," *Metall Mater Trans A*, vol. 52, no. 11, p. 5107–5122, 2021.
- [25] F. Rumiche, J. E. Indacochea and M. L. Wang, "Assessment of the Effect of Microstructure on the Magnetic Behavior of Structural Carbon Steels Using an Electromagnetic Sensor," *J. of Materi Eng and Perform*, vol. 17, no. 4, p. 586–593, 2008.
- [26] B. Gonzalez-Vizcarra, F. Mesa, A. Delgado-Hernandez, M. Avila-Puc and al, "Microstructure and mechanical properties correlation for the steel: A comparative methodology of educational research for physics and mechanical engineering trainings," *Int. J. Phys. Sci.*, vol. 12, no. 23, p. 322–328, 2017.
- [27] J. Yang, R. Li, L. Chen, Y. Hu and Z. Dou, "Research on equipment corrosion diagnosis method and prediction model driven by data," *Process Safety and Environmental Protection*, vol. 158, p. 418–431, 2022.
- [28] C. Örnek, J. Walton, T. Hashimoto, T. S. Ladwein, S. B. Lyon and D. L. Engelberg, "Characterization of 475°C Embrittlement of Duplex Stainless Steel Microstructure via Scanning Kelvin Probe Force Microscopy and Magnetic Force Microscopy," *J. Electrochem. Soc.*, 2017, vol. 164, no. 6, pp. , vol. 164, no. 6, p. C207–C217, 2017
- [29] M. S. Reddy, D. Ponnamma, K. Sadasivuni, S. Aich, S. Kailasa and al, "Sensors in advancing the capabilities of corrosion detection: A review," *Sensors and Actuators A: Physical*, vol. 332, p. 113086, 2021.
- [30] R. Wasif, M. O. Tokhi, J. Rudlin, G. Shirkoohi and F. Duan, "Reliability Improvement of Magnetic Corrosion Monitor for Long-Term Applications," *Sensors*, vol. 23, no. 4, p. 2212, 2023.
- [31] V. F. Novikov, Y. V. Paharukov, A. M. Chehunova, F. K. Shabiev and K. R. Muratov, "Influence of Heat Treatment on Magnetic and Mechanical Properties of Steel 10HSND," *IOP Conf. Ser.: Mater. Sci. Eng.*, vol. 154, p. 012036, 2016.
- [32] A. Elyasigorji, M. Rezaee and A. Ghorbanpoor, "Magnetic Corrosion Detection in Concrete Structures," in *International Conference on Sustainable Infrastructure 2019*, Los Angeles, California: American Society of Civil Engineers, 2019.
- [33] B. Fernandes, M. Titus, D. K. Nims, A. Ghorbanpoor and V. K. Devabhaktuni, " Practical assessment of magnetic methods for corrosion detection in an adjacent precast, prestressed concrete box-beam bridge," *Non-destructive Testing and Evaluation*, vol. 28, no. 2, p. 99–118, 2013.
- [34] M. Jancula, M. Neslusan, F. Pastorek, M. Pitonak, V. Pata, P. Minarik and J. Gocal, "Monitoring of corrosion extent in steel S460MC by the use of magnetic Barkhausen noise emission," *J. Nondestruct. Eval.*, vol. 40, no. 69, 2021.
- [35] M. Neslusan, F. Bahleda, P. Minarik, K. Zgutova and M. Jambor, "Non-destructive monitoring of corrosion extent in steel rope wires via Barkhausen noise emission." *Journal of Magnetism and Magnetic Materials*, vol. 484, p.179-187, 2019.
- [36] F. Pastorek, M. Decky, M. Neslusan and M. Pitonak, "Usage of Barkhausen noise for assessment of corrosion damage on different low alloyed steels," *Appl. Sci.*, vol. 11, 10646, 2021.

- [37] F. Bahleda, M. Neslusan, F. Pastorek, R. Konar and T. Kubjatko, "Barkhausen noise emission as a function of tensile stress in low-alloyed steels: influence of corrosion and steel strength," *Appl. Sci.*, vol. 13, 6574, 2023.
- [38] B. Ducharne, Y. A. Tene Deffo, S. Zhang, G. Sebald, M. Lallart, T. Uchimoto, T. Gallais and O. Ghibaudo, "Carburization depth evaluation from magnetic non-destructive testing," *NDT & E International*, vol. 137, p. 102864, 2023.
- [39] B. Ducharne, Y. A. Tene Deffo, G. Sebald, T. Uchimoto, T. Gallais and O. Ghibaudo, "Low-frequency incremental permeability for the evaluation of deep carburization treatments: Theoretical understanding," *Journal of Magnetism and Magnetic Materials*, vol. 586, p. 171236, 2023.
- [40] B. Ducharne, G. Sebald, H. Petitpré, H. Lberni, E. Wasniewski and F. Zhang, "Magnetic Signatures and Magnetization Mechanisms for Grinding Burns Detection and Evaluation," *Sensors*, vol. 23, no. 10, p. 4955, 2023.
- [41] S. M. Mahbodur, K. Ehsanul and M. D. Shahriar, "Effect of Heat Treatment on Low Carbon Steel: An Experimental investigation," *Applied Mechanics and Materials*, vol. 860, pp. 7-12, 2016.
- [42] H. Krungkarnchana and C. Kongvarhodom, "Low temperature corrosion: Oxidation of carbon steel and stainless steel in air," *Applied Science and Engineering Progress*, vol. 12, no. 1, pp. 44-51, 2017.
- [43] F. S. Ahmed, M. A. El-Zomor, M. S. Ghazala and N. Elshaer R., "Effect of oxide layers formed by thermal oxidation on mechanical properties and NaCl-induced hot corrosion behavior of TC21 Ti-alloy," *Scientific reports*, vol. 12, no. 19265, 2022.
- [44] M. Krajewski, M. Tocarczyk, S. Lewinska and al, "Impact of Thermal Oxidation on Morphological Structural and Magnetic Properties of Fe-Ni Wire-Like Nanochains," *Metallurgical and Materials Transactions A*, vol. 52A, pp. 3530-3540, 2021.
- [45] S. Larose and R. A. Rapp, "Review of low-temperature oxidation of carbon steels and low-alloy steels for use as high-level radioactive waste package materials," Nuclear Regulatory Commission Contract NRC-02-93-005, Ohio, 1997.
- [46] S. Weerakul, F. R. Steward, T. Rirkomboon and al, "Kinetics of oxide formation on carbon steel surface in the presence of oxygen nitrogen mixtures," *Chemical Engineering Transactions*, vol. 29, p. 973-978, 2012.
- [47] W. H. Vernon, T. J. Nurse, C. J. Clews and E. A. Calnan, *Nature, Lond.*, vol. 164, no. 910, 1949.
- [48] W. H. Vernon, E. A. Calnan, C. J. Clews and T. J. Nurse, "The oxidation of iron around 200°C," *Proc. R. Soc. Lond. A*, vol. 216, pp. 375-397, 1953.
- [49] D. Davies, U. R. Evans and J. Agar, *Proceedings of the Royal Society of London*, vol. A225, no. 443, 1954.
- [50] T. Islam and H. M. Rashed, "Classification and Application of Plain Carbon Steels," *Reference Module in Materials Science and Materials Engineering*, p. B9780128035818103000, 2019.
- [51] K. Tsutsui, H. Terasaki, K. Uto, T. Maemura, S. Hiramatsu, K. Hayashi, K. Moriguchi and S. Morito, "A methodology of steel microstructure recognition using SEM images by machine learning based on textural analysis," *Materials Today Communications*, vol. 25, p. 101514, 2020.
- [52] R. B. Runk and H. J. Kim, *Oxidation of Metals*, vol. 2, no. 3, 1970.
- [53] N. Zettili, *Quantum mechanics: concepts and applications*, 2. ed., Ed., Chichester, U.K.: Wiley, 2009.
- [54] J. J. Sakurai and J. Napolitano, *Modern quantum mechanics*, 3. ed., Ed., Cambridge, U.K.: Cambridge University Press, 2021.
- [55] B. D. Cullity and C. D. Graham, *Introduction to magnetic materials*, 2. ed., Ed., Hoboken, New Jersey: IEEE/Wiley, 2015.
- [56] X. Bi, C. Qiu, F. Qin, J. Huang and H. Yuan, "Controlling Exchange Interactions and Emergent Magnetic Phenomena in Layered 3 d-Orbital Ferromagnets," *Advanced Physics Research*, vol. 2, no. 6, p. 2200106, 2023.

- [57] D. Negri, A. Paoluzi and L. Pareti, "Magnetic anisotropy and magnetisation processes in 3:29, 1:12 and 2:17 type Nd:(Fe, Co, Ti) related compounds," *Journal of Magnetism and Magnetic Materials*, vol. 239, no. 3, p. 302–310, 2004.
- [58] H. Tsukahara, K. Iwano, T. Ishikawa, C. Mitsumata and K. Ono, "Relationship between magnetic nucleation and the microstructure of a hot-deformed permanent magnet: micromagnetic simulation," *NPG Asia Mater*, vol. 12, no. 1, p. 29, 2020.
- [59] A. Awadallah, S. H. Mahmood, Y. Maswadeh, I. Bsoul and A. Aloqaily, "Structural and magnetic properties of vanadium doped M-type barium hexaferrite (BaFe_{12-x}V_xO₁₉)," *IOP Conference Series: Materials Science and Engineering*, 2015, vol. 92, no. 1, p. 012006, 2015.
- [60] T. L. Manh, J. A. Benitez, J. H. Hernandez and M. Hallen J., *Barkhausen noise for non-destructive testing and materials characterization in low carbon steels*, Oxford: Woodhead Publishing series in electronic and optical materials, 2000.
- [61] Y. Hou, X. Li, Y. Zheng, J. Zhou, J. Tan and X. Chen, "A Method for Detecting the Randomness of Barkhausen Noise in a Material Fatigue Test Using Sensitivity and Uncertainty Analysis," *Sensors*, vol. 20, no. 18, p. 5383, 2020.
- [62] P. Fagan, B. Ducharne, L. Daniel and A. Skarlatos, "Multiscale modelling of the magnetic Barkhausen noise energy cycles," *Journal of Magnetism and Magnetic Materials*, vol. 517, p. 167395, 2021.
- [63] A. Yashan, G. Dobmann, F. Kojima, T. Takagi, S. S. Udpa and J. Pávó, "Measurements and semi-analytical modeling of incremental permeability using eddy current coil in the presence of magnetic hysteresis," *Electromagnetic Non-destructive Evaluation*, pp. 150-157, 2002.
- [64] T. Matsumoto, T. Uchimoto, T. Takagi, G. Dobmann, B. Ducharne, S. Oozono and H. Yuya, "Investigation of electromagnetic non-destructive evaluation of residual strain in low carbon steels using the eddy current magnetic signature (EC-MS) method," *Journal of Magnetism and Magnetic Materials*, vol. 479, pp. 212-221, 2019.
- [65] D. C. Jiles, "Magnetic properties and microstructure of AISI 1000 series carbon steels," *J. Phys. D: Appl. Phys*, vol. 21, pp. 1186-1 195, 1988.
- [66] H. Choudhary, M. Shahriar, B. Bhallamudi and S. Singh, "Cyclic Heat Treatment of Carbon Steel," *International Journal of Innovative Science and Research Technology*, vol. 7, no. 6, pp. 1198-1204, 2022.
- [67] M. R. Longhitano, F. Sixdenier, R. Scorretti, L. Krähenbühl and C. Geuzaine, "Temperature-dependent hysteresis model for soft magnetic materials," *The international journal for computation and mathematics in electrical and electronic engineering*, 2019.